UNIVERSITY OF CALIFORNIA SAN DIEGO

# Phase Separation and Fibrillization of Human Annexin A7 is mediated by its proline-rich domain

A Thesis submitted in partial satisfaction of the requirements
for the degree Master of Science

in

Chemistry

by

Chenrong Yu

Committee in charge:

Professor Lalit Deshmukh, Chair
Professor Itay Budin
Professor Patricia A. Jennings

2023

The Thesis of Chenrong Yu is approved, and it is acceptable in quality and form for publication on microfilm and electronically.

University of California San Diego

2023

# DEDICATION

I dedicate this thesis to the following people:

My methor, Professor Lalit Deshmukh, for offering me an opportunity to work on this exciting project. My committee members, Professor Patricia A. Jennings and Professor Itay Budin, for providing helpful suggestions and constructive feedback.

My parents, Weimin and Suyun, for believing in me and for their unconditional love.

My friends and roommates, for their encouragement and support.

All the members of Deshmukh lab, for their help and support.

TABLE OF CONTENTS

LIST OF FIGURES

LIST OF TABLES

## LIST OF ABBREVIATIONS

| | |
|---|---|
| A7 | Annexin A7 |
| A11 | Annexin A11 |
| AD | Alzheimer's disease |
| ALG-2 | Apoptosis-linked gene-2 |
| ALIX | Apoptosis-linked gene-2-interacting protein X |
| ALS | Amyotrophic lateral sclerosis |
| BME | β-mercaptoethanol |
| CR | Congo red |
| DIC | Differential interference contrast |
| DMSO | Dimethylsulfoxide |
| DOPC | 1,2-dioleoyl-sn-glycero-3-phosphocholine |
| DOPS | 1,2-dioleoyl-sn-glycero-3-phospho-L-serine |
| FRAP | Fluroscence recovery after photobeleaching |
| FTD | Frontotemporal dementia |
| FUS | Fused in sarcoma |
| GB1 | B1 domain of protein G |
| GdmCl | Guanidine hydrochloride |
| GUV | Giant unilamellar vesicles |
| HEPES | N-2-hydroxyethylpiperazine-N'-2-ethanesulfonic acid |
| hnRNPA1 | heterogeneous nuclear ribonucleoprotein |
| HPLC | High-performance liquid chromatography |
| IPTG | Isopropyl β-d-1-thiogalactopyranoside |

| | |
|---|---|
| LB | Luria-Bertani |
| LLPS | Liquid - liquid phase seperation |
| Liss Rhod PE | 1,2-dipalmitoyl-sn-glycero-3-phosphoethanolamine-N-(lissamine rhodamine B sulfonyl) |
| MS | Mass spectrometry |
| NMR | Nuclear magnetic resonance |
| PD | Parkinson's disease |
| PRD | Proline-rich domain |
| PTMs | Posttranslational modifications |
| SD | Standard deviation |
| SDS-PAGE | Sodium dodecyl-sulfate polyacrylamide gel electrophoresis |
| SODD | Suppressor of death domains |
| S100A6 | Calcyclin |
| TCEP | Tris (2-carboxyethyl) phosphine |
| TEM | Transmission electron microscopy |
| TEV | Tobacco etch virus |
| ThT | Thioflavin T |

ACKNOWLEDGEMENTS

I am deeply grateful to my mentor, Prof. Lalit Deshmukh, for his support and guidance. Without his help, I would not be able to finish this project. I also want to thank Prof. Patricia A. Jennings and Itay Budin for their help and constructive feedback.

I want to thank my wonderful lab mates, Spencer L. Nelson, Ruben D. Elias, and Aman Shihora, for their clear explanations and advice. I thank Dr. Rodolfo Ghirlando for collecting analytical ultracentrifugation data on annexin A7. I thank Dr. Peng Guo for his help with confocal microscopy. I thank Dr. Andre Guillermo and Dr. Ying Jones for their help with electron microscopy experiments. I thank Dr. Jake B. Bailey for his guidance on X-ray diffraction measurements. I want to thank Dr. Nicolas-Frédéric Lipp and Alexander Harjung for their help with making lipid vesicles.

I want to thank my parents for their unconditional love and support, which allowed me to focus on my research and not be afraid of failure. Lastly, I would like to express my deep gratitude to my friends and roommates for providing me emotional support.

Chapter 1, in full, has been submitted for publication of the material as it may appear in Biochemistry, Yu, Chenrong, Nelson, Spencer, L., Ghirlando, Rodolfo, Deshmukh, Lalit. "Phase separation and fibrillization of human annexin A7 is mediated by its proline-rich domain". The author of the thesis was the primary researcher and author of this paper.

# VITA

2021 Bachelor of Science in Biomolecular Science, University of Michigan, Ann Arbor

2023 Master of Science in Chemistry, University of California San Diego

# PUBLICATIONS

**Yu, C.**; Nelson S. L.; Ghirlando, R.; Deshmukh; L., Phase separation and fibrillization of human annexin A7 is mediated by its proline-rich domain. Under submission.

ABSTRACT OF THE THESIS

Phase Separation and Fibrillization of Human Annexin A7 is mediated by its proline-rich domain

by

Chenrong Yu

Master of Scienc in Chemistry

University of California San Diego, 2023

Professor Lalit Deshmukh, Chair

Annexins are a large superfamily of calcium- and phospholipid-binding proteins that regulate many membrane-related cellular events. Annexins consist of a variable N-terminal "head" domain, which confers their functional specificity, and a conserved C-terminal core comprising multiple copies of a globular "annexin repeat" that harbors calcium- and membrane-binding sites. Among the 12 human annexins, annexin A7 contain unusually long head domain

(180 residues), which is predicted to be disordered. This highly conserved proline-rich domain (PRD, ~25% proline residues) comprises binding sites for multiple cellular proteins, namely sorcin, suppressor of death domains (SODD), and apoptosis-linked gene-2 (ALG-2), and these interactions are suggested to regulate the biological functions of A7, including calcium homeostasis, tumor suppression, apoptosis, and plasma membrane repair. Additionally, the extreme N-terminal residues ofA7-PRD regulate membrane aggregation and fusion events and self-association of A7 in the presence of calcium. Using microscopy and dye-binding assays, we show that recombinant A7 and its isolated PRD spontaneously phase separate into spherical condensates, which slowly transition into β-sheet–rich fibrils. We establish that fibrillization of A7-PRD proceeds via primary nucleation and fibril-catalyzed secondary nucleation processes, as determined by chemical kinetics, providing a mechanistic basis for its amyloid assembly. This study confirms and highlights a subclass of eukaryotic PRDs prone to forming aggregates with important physiological and pathological implications.

# INTRODUCTION

## Section 1: Protein Phase Separation and Fibrillization

To carry out cellular functions, cells rely on the compartmentalization of biomolecules. Such compartments comprise membrane-enclosed organelles (e.g., mitochondria, nucleus, golgi, and endoplasmic reticulum), where well-defined lipid membranes separate the components of these organelles from their surroundings. Additionally, cells contain membraneless organelles (e.g., nucleolus, nuclear speckles, stress granules, and P-bodies), which lack membranes but still confine a multitude of biomolecules, including proteins, enzymes, and nucleic acids, within a boundry.[1-3] Unlike membrane-enclosed organelles, the components of membraneless structures can rapidly exchange with the cellular milieu. Such membraneless structures can also dissolve, thereby dispersing their contents into the surrounding environment. Although many such membraneless organelles were discovered and identified decades or even centuries ago (e.g., the nucleolus was known since the 1830s)[4], it has only been in recent years that we have begun to understand the underlying molecular processes that orchestrate their formation and dissolution. For example, these structures are primarily controlled by dynamic intermolecular interactions between their components, by changes in pH, and by posttranslational modifications (PTMs) that exert spatiotemporal control.[5-6] Emerging evidence indicates that these structures are formed by a physical process called liquid-liquid phase separation (LLPS) or phase transition (Fig. 1), where a solution comprising different polymers forms a two-phase system that has lower energy than the corresponding fully mixed state.[8-9] Therefore, these membraneless structures, also known as biomolecular condensates, possess liquid-like characteristics, including a spherical shape, the ability to fuse with one another, and the ability to deform under stress. In the past few years, multiple cellular processes that are controlled by these condensates have been identified, including

stress response, immune signaling, gene expression, and neurotransmission. Moreover, accumulating evidence has hinted towards the involvement of these biomolecular condensates in the progression of disease, including cancer and neurodegenerative disorders.[10-11] These discoveries have given rise to a new field focused on understanding the organization, properties, and regulation of these membraneless organelles, their function, and their relationship with the corresponding pathology.

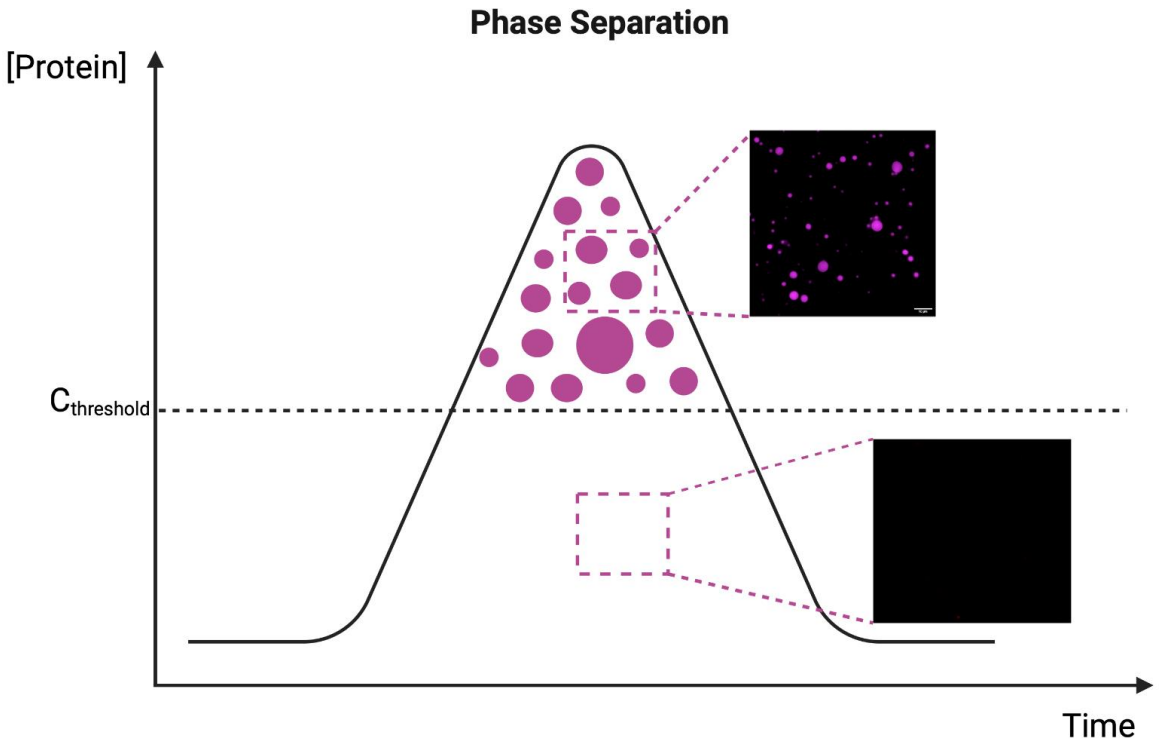


**Figure 1. Schematic of protein phase separation.** LLPS of proteins results in the formation of two phases: a dense phase (green spheres) that is enriched in proteins and a dilute phase that represents the surrounding medium. It is a concentration-dependent process driven by the minimization of the global free energy of the system and only occurs above a threshold concentration of the involved proteins ($C_{threshold}$, represented by a dashed line). Adapted from Alberti et al.[7]

Although cellular condensates are enriched with numerous proteins and RNAs, often only a small subset is needed to reconstitute such compartments in vitro.[9] Remarkably, in some cases,

such in vitro condensates become rigid over time, resulting in the formation of amyloid-like fibers (Fig. 2). For example, proteins such as fused in sarcoma (FUS), heterogeneous nuclear ribonucleoprotein A1 (hnRNPA1), and others have been shown to form dynamic condensates that slowly transform into fibrous structures.[12-13] The underlying molecular details of these liquid-to-solid transitions are not clear and are the subject of intense investigation. This is because amyloid fibrils are commonly associated with proteinopathies, including Alzheimer's disease and Parkinson's disease (AD and PD, respectively),[14] and several key proteins involved in these proteinopathies undergo LLPS in vivo and in vitro. Moreover, disease-associated mutations in many of these proteins [e.g. frontotemporal dementia (FTD)-associated FUS, AD-associated Tau, amyotrophic lateral sclerosis (ALS)-associated TDP-43, PD-associated α-synuclein etc.] were shown to accelerate the formation of their pathological aggregates,[11, 13, 15] suggesting that these aggregates may stem from aberrant changes in physiological phase separation. Note that whether biological condensates possess the intrinsic property to form such pathogenic aggregates or whether such aggregates are the nucleation-related end-products of some of the transient conformations or oligomers that may form within these condensates is currently not known.

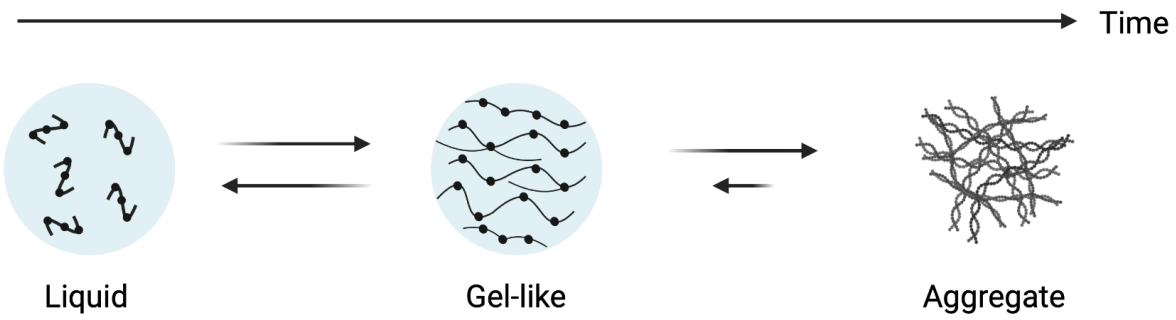


**Figure 2. Liquid-to-solid transitions of biological condensates.** The time-dependent maturation of biological condensates can lead to rigid structures, including gel-like intermediates and fibrillar aggregates. Adapted from Zbinden et al.[11]

A key feature of phase-separating proteins is the multivalency of intramolecular and intermolecular interactions,[9, 16] which promote phase separation at lower threshold concentrations of the involved proteins (cf. Fig. 1). Such interactions can be exerted by folded proteins that oligomerize, RNA-biniding proteins, proteins with tandem globular repeats, and proteins harboring disordered regions and/or disordered domains with low sequence complexity (Fig. 3).[9, 17] The latter are highly abundant in cellular condensates and are known to tune their formation and dissolution via charge-charge, charge-π, and π-π stacking interactions and via cellular PTMs. In these regards, our laboratory is especially interested in proline-rich domains (PRDs) and in recent years, we have investigated many such domains that fulfill the following criteria: ≥ 160 total amino acids comprising ≥ 25% proline residues.[18-21] This is because PRDs are extremely abundant in eukaryotes and play a vital role in signal transduction due to their disordered nature and

multivalency, which yield favorable binding properties.[18] Despite their importance, PRDs are not

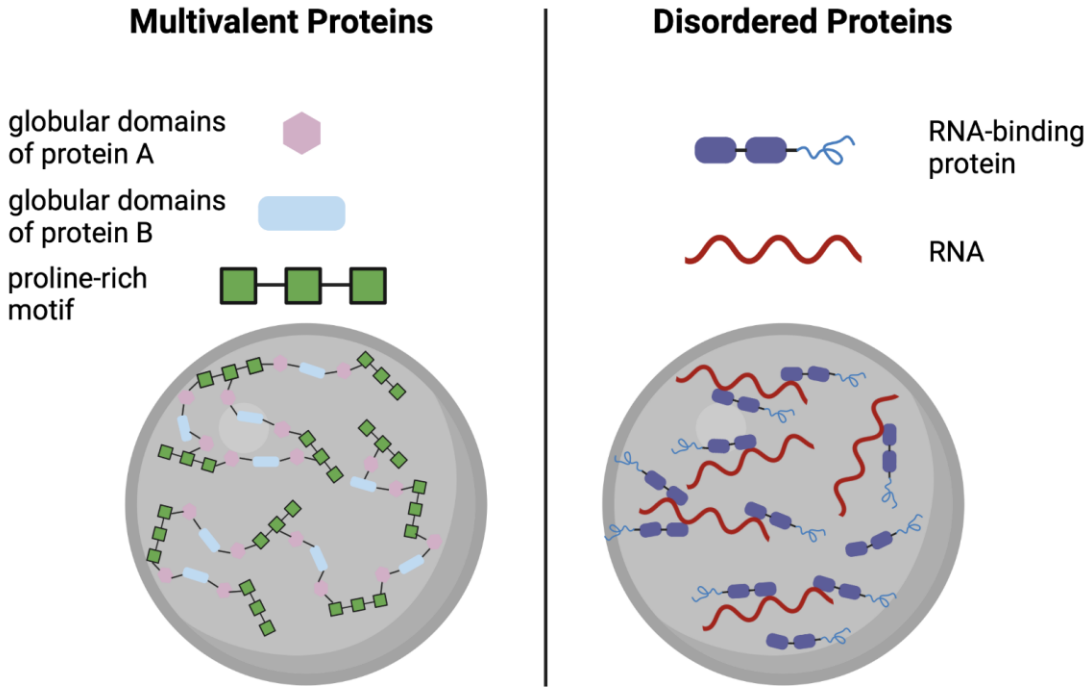


**Figure 3. Intermolecular features of phase separation.** Types of intermolecular interactions that drive the formation of biomolecular condensates. Adapted from Shin and Brangwynne.[9]

often studied by biophysical methods due to problems associated with their recombinant expression and their lack of a well-defined fold, which prevents their investigation by structural namely X-ray crystallography and cryo-electron microscopy (EM). Additionally, because of the lack of amide protons in proline residues, PRDs are difficult to study by conventional proton-detected solution nuclear magnetic resonance (NMR) spectroscopy methods. An accidental discovery in our laboratory, however, established that a PRD of human protein ALIX (166 residues, 30% prolines) phase separates into nondynamic condensates and forms labile amyloid fibrils that dissolve and reform upon Src-kinase mediated tyrosine phosphorylation of this domain.[18-20] Moreover, we recently showed that monoubiquitination of recombinant ALIX via

NEDD4-family E3 ligases promotes its fibrillization.[22] This is because ALIX also carries a ubiquitin-binding domain that promotes intermolecular interactions between monoubiquitinated ALIX, thereby accelerating its fibrillization via its amylodogenic PRD. We therefore want to identify and characterize other similar PRDs in the human proteome that can phase separate and form amyloid fibrils. Additionally, we want to understand the mechanistic underpinnings and structural details of how PRDs can phase separate and form cross-β-sheet rich amyloid structures.

**Section 2: Annexins and Annexin A7**

Annexins are ubiquitously expressed calcium-dependent membrane-binding proteins.[23-25] Humans carry 12 annexins (1–11 and 13; Fig. 4), which play vital roles in essential cellular processes such as calcium homeostasis, cell migration, apoptosis, tumor suppression, and many others. All annexins comprise multiple copies of a conserved structural core known as an annexin repeat, a ~70 residue-long globular domain harboring five α-helices. The annexins bind to calcium and negatively charged phospholipids via their annexin repeats, which are extensively studied by structural methods, including X-ray crystallography and solution NMR spectroscopy. Additionally, annexins contain N-terminal head domains that are characterized by their sequential diversity and variable length (ranging from 10 to 200 residues). Among annexins, annexin A7 and A11 comprise the longest N-terminal domains that are rich in proline residues (180 and 196 residues, 25% and 30% prolines, respectively). These PRDs are likely disordered, bind to multiple cellular proteins,[26] and are implicated in the formation of membraneless organelles.[27] Moreover, a cellular study linked four missense point-mutations in the PRD of annexin A11 in individuals affected with ALS, a fatal motor-neurone disease,[29] and showed that these mutations result in abundant neuronal deposition of A11 in ALS patients. A recent study from our laboratory showed that A11-PRD and its ALS-associated variants formed spherical condensates that slowly

transitioned into β-sheet–rich amyloid fibrils.[21] Surprisingly, these fibrils dissolved in the presence of S100A6, an A11-binding partner overexpressed in ALS. In contrast to A11-PRD, its ALS-associated variants exhibited slower fibrillization, but S100A6-mediated dissolution of their fibrils was also slower, providing a molecular basis for A11 inclusions and S100A6 overexpression observed in ALS. Because the N-terminal head domain of annexin A7 is also rich in proline residues (180 residues with 25% prolines), we asked whether A7 and its PRD undergo phase separation and fibrillization.

Annexin A7, also known as synexin, was the first reported annexin and was originally identified to promote calcium-dependent aggregation of chromaffin granules.[30-31] It is involved in calcium homeostasis, plasma membrane repair, apoptosis, tumor progression, and inflammatory myopathies. The highly conserved head domain of A7 comprises binding sites for multiple cellular proteins, namely sorcin[32], suppressor of death domains (SODD)[33], and apoptosis-linked gene-2 (ALG-2)[34-35], and these interactions are suggested to regulate the biological functions of A7. Additionally, the extreme N-terminal residues of its head domain regulate A7-mediated membrane aggregation and fusion events[36-37] and its self-association in the presence of calcium.[33] In this study, we characterized the aggregation properties of A7 and show that recombinant full-length A7 and its isolated PRD form spherical condensates that mature into β-sheet–rich amyloid fibrils. A7-PRD is therefore likely responsible for these aggregation properties. Additionally, we identified molecular processes involved in the fibrillization of A7-PRD using quantitative chemical kinetics. Although the cellular processes and corresponding pathologies related to these

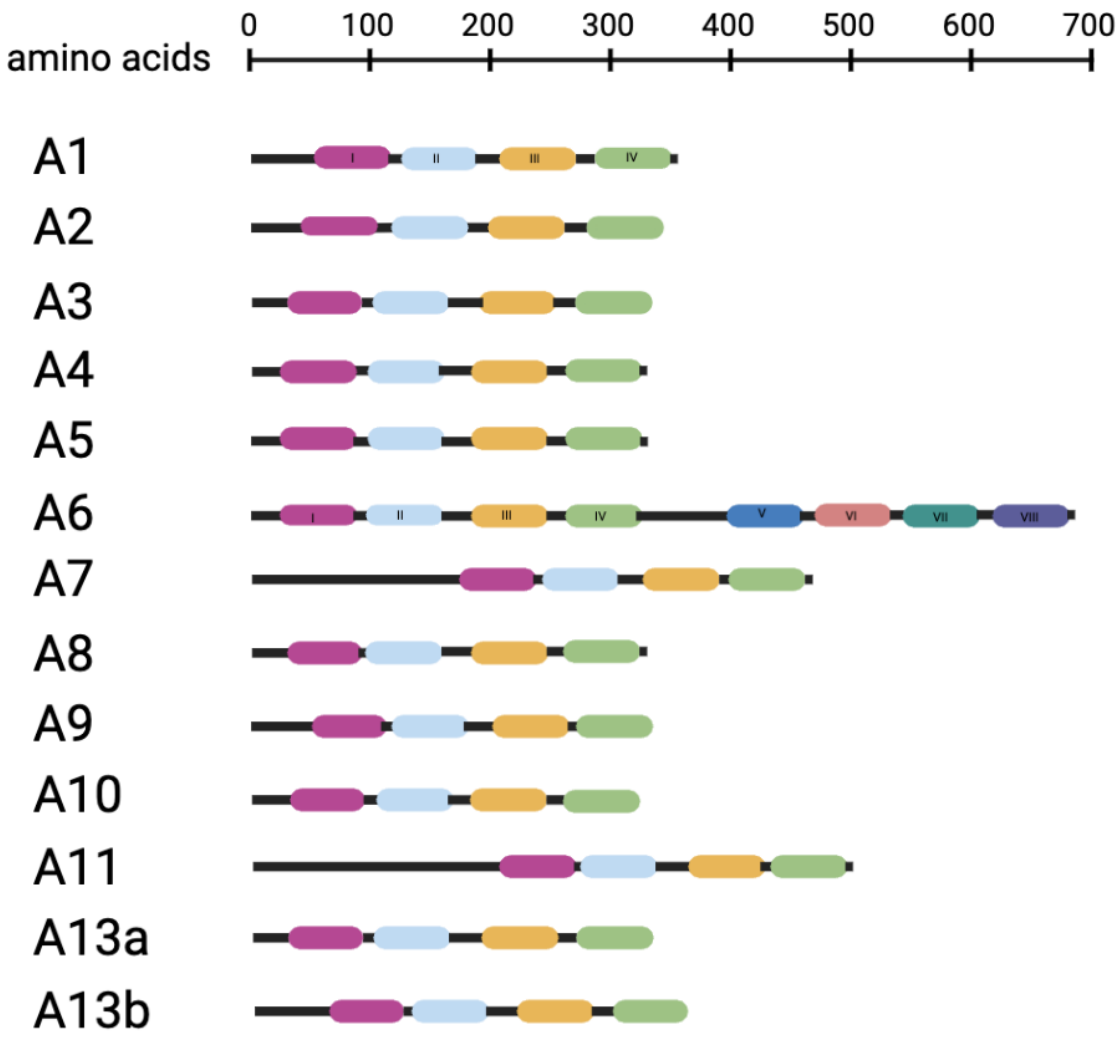


**Figure 4. Structural organization of human annexins.** Globular annexin repeats and N-terminal head domains are shown as cylinders and lines, respectively. Adapted from Enrich et al.[28]

aggregation properties of A7 are not known and are the topic of an ongoing investigation in our laboratory, this study confirms and highlights a subclass of eukaryotic PRDs prone to forming aggregates.

CHAPTER 1

**Phase separation and fibrillization of human annexin A7 is mediated by its proline-rich domain.**

Annexins are a large superfamily of calcium- and phospholipid-binding proteins that regulate many membrane-related cellular events.[23-24] Annexins consist of a variable N-terminal "head" domain, which confers their functional specificity,[25] and a conserved C-terminal core comprising multiple copies of a globular "annexin repeat" that harbors calcium- and membrane-binding sites. Among the 12 human annexins, A7 and A11 contain unusually long head domains (180 and 196 residues, respectively), which are predicted to be disordered and have short peptide motifs that bind to specific intracellular protein partners.[26, 33] The highly conserved head domain of A7 (Fig. 8) comprises binding sites for multiple proteins, namely sorcin[32], suppressor of death domains (SODD)[33], and apoptosis-linked gene-2 (ALG-2)[34-35], and these interactions are suggested to regulate the biological functions of A7, including calcium homeostasis, tumor suppression, apoptosis, and plasma membrane repair. Additionally, the extreme N-terminal residues of the head domain regulate A7-mediated membrane aggregation and fusion events[36-37] and its self-association in the presence of calcium.[33] Similarly, the head domain of A11 binds to S100A6 (calcyclin),[21, 38] and is involved in creating cerebral A11 inclusions in patients with a fatal motor-neuron disease, amyotrophic lateral sclerosis (ALS).[29] We recently established that the head domain of annexin A11 phase separates into spherical condensates in vitro, which slowly transition into β-sheet–rich amyloid fibrils.[21] Although there is little sequence similarity between the head domains of A7 and A11 (Fig. 9), like A11, the A7-head domain is rich in proline residues (Fig. 5A–B). Thus, here we investigated its aggregation properties and show that this proline-rich domain (PRD) induces the phase separation and fibrillization of A7.

Fig. 10 lists the recombinant A7 constructs used in the current study, including full-length A7 and its truncated fragments representing A7-PRD. Sedimentation velocity experiments established that, in the absence of calcium and at low concentrations (≤15 μm), recombinant A7 was predominantly monomeric (Figs. 5C and 11). To probe its membrane-binding properties, we monitored the colocalization of A7 with giant unilamellar vesicles (GUVs) using confocal microscopy. ATTO-647N-labeled A7 (200 nM) was incubated with GUVs comprising zwitterionic DOPC and fluorescent Liss Rhod PE in the presence of calcium. Under these conditions, no fluorescence signal from A7 was observed at the membrane surface, establishing that A7 did not colocalize with these zwitterionic GUVs (Fig. 12). Similarly, in the absence of calcium, A7 did not colocalize with GUVs comprising DOPC and negatively charged DOPS (Fig. 5D). However, a robust and uniform colocalization of A7 was observed with anionic GUVs in the presence of 100 nM calcium. These observations establish that recombinant A7 associates with anionic membranes in a calcium-dependent manner. These results are consistent with original reports that showed that A7 is a calcium-dependent membrane binding protein[39-40] and establish that the recombinant A7 made here is functionally relevant.

At concentrations ranging between 30–40 μM and in the presence of calcium, the solution of A7 became cloudy. Microscopy examination revealed the presence of spherical condensates (Fig. 6A; note that recombinant A7 is not soluble above 40 μM and undergoes visible precipitation). A7 condensates rarely fused, suggesting their nondynamic nature. Poor fluorescence recoveries after photobleaching (FRAP) were observed for A7 condensates (~10% average recovery in 75 s, Fig. 6B), further confirming their nondynamic character. To determine whether A7 condensates transition into amyloid fibrils, we monitored aggregation kinetics using an amyloid-sensitive dye, Thioflavin T (ThT). A7 samples ($n$ = 3) were incubated with calcium at 37 °C for ~70 h, and the

ThT signal was recorded with continuous linear shaking. All A7 samples exhibited sigmoidal aggregation profiles consisting of an initial dip in ThT signals, followed by lag, growth, and plateau phases, a hallmark of amyloid formation,[41] with ~40 h to reach half-maximal signal ($t_{1/2}$; Fig. 6C). Further analysis of these samples at the plateau phase by transmission electron microscopy (TEM) revealed the presence of rope-like amyloid fibrils (Fig. 6C). Collectively, these results establish that recombinant A7 spontaneously phase separates in the presence of calcium and undergoes a slow time-dependent fibrillization under mechanical agitation.

To determine the role of A7-PRD on the phase separation and fibrillization properties of A7, we used two truncated constructs, $A7^{Strep}_{PRD}$ and $A7_{PRD}$. Both constructs carried a cleavable N-terminal fusion tag comprising the B1 domain of protein G, followed by a polyhistidine affinity tag and a TEV-protease cleavage site (Fig. 10). Additionally, $A7^{Strep}_{PRD}$ carried a non-cleavable strep affinity tag at the C terminus, engineered to facilitate Alexa-Fluror488 labeling for fluorescence microscopy. The latter showed that $A7^{Strep}_{PRD}$ (50 μM) readily phase separated in the presence of calcium (Fig. 7B). Similar condensates were observed for $A7_{PRD}$ using DIC imaging (Fig. 13). Fresh condensates of $A7^{Strep}_{PRD}$ showed ~50% average FRAP recoveries in 125 s, indicating that, unlike its full-length counterpart, condensates of $A7^{Strep}_{PRD}$ were relatively more dynamic, likely because of rapid cycling between its phase-separated and soluble states. The nondynamic nature of the condensates of recombinant A7 perhaps stems from other intermolecular interactions absent in its truncated counterpart. Note that the increased gelation of full-length A7 relative to its PRD is consistent with our recent observations with the human protein ALIX, where we showed that condensates of full-length ALIX were relatively more gel-like compared to those of its isolated PRD.[20] Solutions of both $A7^{Strep}_{PRD}$ and $A7_{PRD}$ condensates underwent visible precipitation over time.

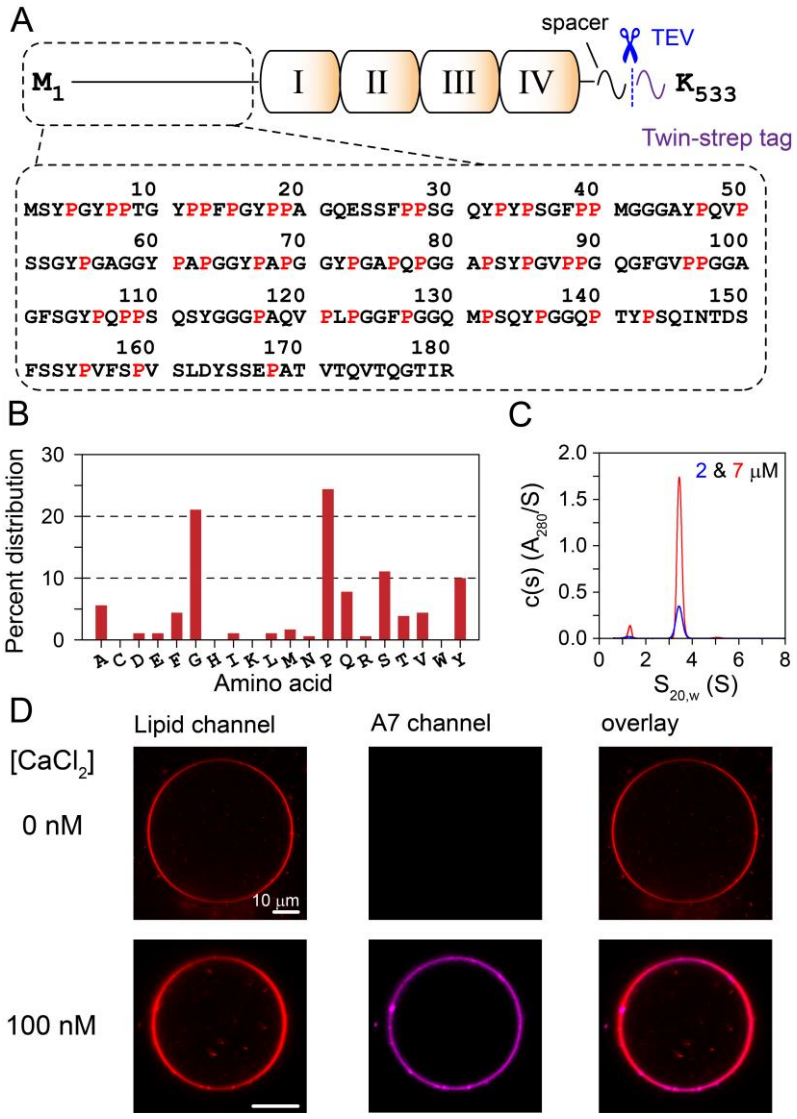


**Figure 5. Full length annexin A7 properties.** (**A**) Scheme of full-length A7 construct used in current study and primary sequence of A7-head domain; I–IV (annexin repeats); prolines (red); twin-strep tag (magenta). TEV protease cleavage site is shown in dashed lines and scissors (blue). (**B**) Amino acid composition of A7-head domain. (**C**) Sedimentation profiles of A7 at 2 and 7 μM (blue and red, respectively). (**D**) Fluorescence microscopy analysis of membrane binding properties of ATTO-647N-labeled A7 (200 nM), in the absence and presence of 100 nM calcium. GUVs were made using DOPC (69.95%) and DOPS (30%) and spiked with 16:1 Liss Rhod PE dye (0.05%). Representative microscopy images of the respective fluorescent channels and their overlay are shown. Results in panels **C**–**D** were acquired with TEV-cleaved A7.

Spectral-shift assays performed using an amyloid-specific dye, Congo red (CR), showed clear red shifts for aged solutions of $A7_{PRD}$, indicating the presence of amyloidogenic aggregates (Fig.

7D).[41] Further analyses of these $A7_{PRD}$ solutions by fluorescence microscopy and TEM revealed ribbon-like fibrils (Figs. 7E and F, respectively). Powder X-ray diffraction of these fibrils showed two rings at 4.69 and 10.34 Å (Fig. 7G), consistent with a cross-β-sheet rich amyloid structure.[42] To further gain a mechanistic understanding of $A7_{PRD}$ amyloid formation, we monitored its aggregation kinetics using ThT assays. In the presence of calcium and under non-agitated conditions at 37 °C, $A7_{PRD}$ exhibited sigmoidal aggregation profiles with a $t_{1/2}$ of ~1 h (Fig. 7I). Therefore, in contrast to recombinant A7 that underwent slow fibrillization under agitated conditions ($t_{1/2}$ ~40 h; cf. Fig. 6C), fibrillization of its isolated PRD was not only ~40-fold faster but also did not require mechanical agitation. Although similar sigmoidal aggregation profiles were obtained in the absence of calcium for $A7_{PRD}$, the corresponding $t_{1/2}$ was notably longer, ~24 h, establishing that calcium accelerates its aggregation. Collectively, the above results show that A7-PRD forms spherical condensates that rapidly mature into β-sheet–rich fibrils and are likely responsible for phase separation and fibrillization of full-length A7.

To elucidate the underlying microscopic processes that contribute to the fibrillization of $A7_{PRD}$, we carried out ThT assays by varying the initial monomer concentrations. Highly reproducible curves with minimal variation between the replicates (n = 2) were obtained at each concentration point, namely 5, 10, 15, 30, and 50 μM (Fig. 14). The high-quality of these datasets facilitated their global fitting using the protocol described by Knowles and colleagues via their online platform, AmyloFit.[43] Briefly, first, the relationship between $t_{1/2}$ and the starting monomer concentration of $A7_{PRD}$ was ascertained by fitting a power-law function, $t_{1/2} \sim [m_0]^{\gamma}$, where $m_0$ and $\gamma$ are the starting monomer concentration and scaling exponent, respectively (Fig. 15). The corresponding $\gamma$ value was -0.66, suggesting that at higher $A7_{PRD}$ concentrations, the $t_{1/2}$ deviates from the ideal power-law function, and therefore, one or more of the processes contributing to $A7_{PRD}$ aggregation, such

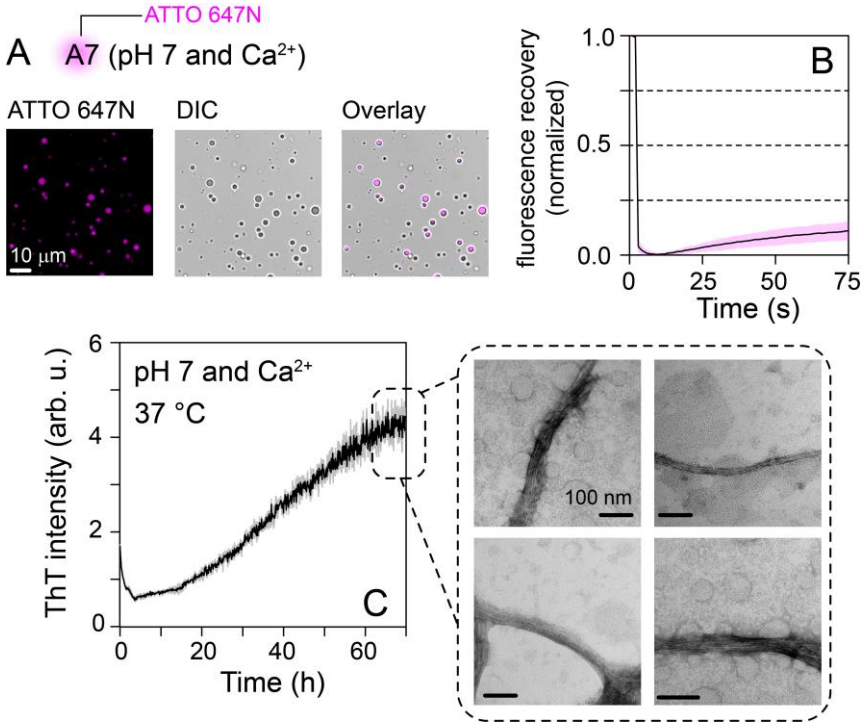


**Figure 6. Full length annexin A7 phase seperation and fibrilization.** (**A**) Microscopy images of condensates of ATTO-647N-labeled A7; DIC = differential interference contrast. (**B**) FRAP curves of A7 condensates; $n$ = 8, mean (solid line), SD (shaded region). (**C**) Aggregation kinetics of A7 (40 μM) monitored using ThT fluorescence; $n$ = 3, mean (solid line), SD (shaded region). Representative TEM images of samples at 70 h are shown on right (dashed square).

as fibril-catalyzed secondary nucleation, become dominant at these concentrations.[44] Next, data fitting was performed where different kinetic models were fit globally to the experimental ThT curves. The model termed "secondary nucleation dominated, unseeded," which incorporates primary and secondary nucleation, along with fibril elongation, adequately replicated experimental ThT curves. Simpler models that did not incorporate secondary nucleation (Fig. 7G; also see Fig. 16 for schematic of individual processes involved in fibrillization) did not fit well. Note that in this secondary nucleation model, the time-dependent formation of fibrils depends on combinations of rate constants, $k_n k_+$ and $k_2 k_+$, where $k_n$ is the rate constant for the formation of primary nuclei, $k_+$ is the fibril elongation rate constant, and $k_2$ is the rate of formation of secondary nuclei (Fig. 16). The

best-fit values were 1.3e+5 $M^{-2}h^{-2}$ and 6.3e+4 $M^{-3}h^{-2}$ for $k_n k_+$ and $k_2 k_+$, respectively. Collectively, these results establish that fibrillization of $A7_{PRD}$ involves both primary and secondary nucleation, with the latter being the dominant process.

In summary, we show that $A7_{PRD}$ phase separates and forms amyloid fibrils in vitro. It is, thus, likely responsible for the phase separation and fibrillization of full-length A7 observed here. A7 is known to self-associate and promote membrane aggregation and fusion events in the presence of calcium.[30-31, 45] Additionally, prior studies have ascribed these properties to the extreme N-terminal residues of $A7_{PRD}$.[33, 36-37] The results presented here are consistent with these known observations. Moreover, the aggregation properties of $A7_{PRD}$ are similar to those of $A11_{PRD}$ despite their limited sequence similarity. We found that the amyloid fibrils formed by $A11_{PRD}$ were labile and slowly dissolved upon the addition of its binding partner, S100A6.[21] Studies to determine whether fibrils of $A7_{PRD}$ exhibit a similar dissolution pattern in the presence of its known binding partners, namely sorcin, SODD, and ALG-2, are currently ongoing in our laboratory. Finally, we note that the aggregation properties of $A7_{PRD}$ are similar to another PRD discovered in our laboratory, belonging to the human protein ALIX, which was shown to phase separate and form amyloid fibrils.[18-20, 22] Therefore, although eukaryotic PRDs are known to create dynamic cell signaling networks, PRDs of A7, A11, and ALIX may represent a new subclass of PRDs that can phase separate and form amyloid fibrils.

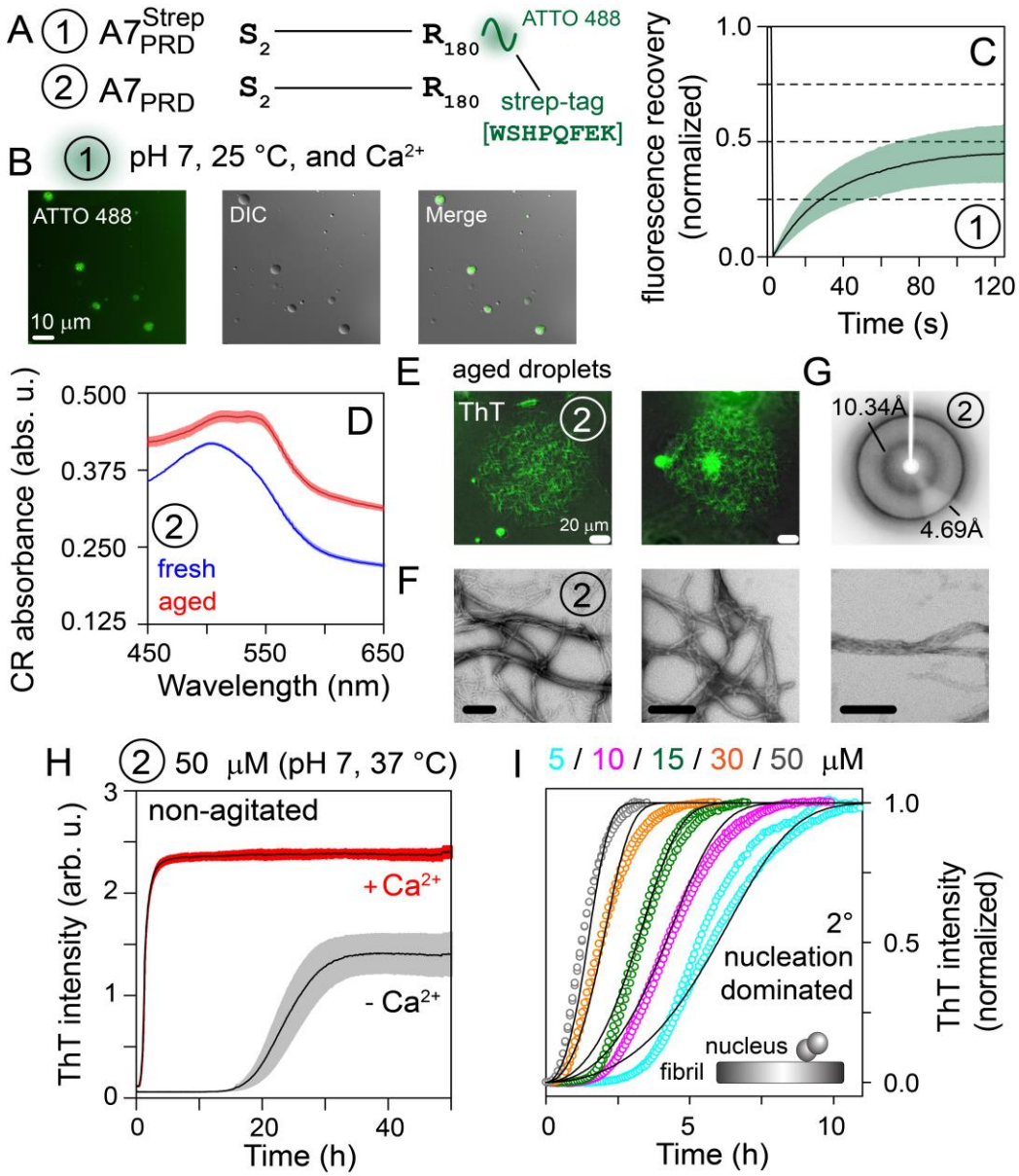


**Figure 7. $A7_{PRD}$ phase seperation and fibrilization.** (**A**) Two A7-PRD constructs tested in this study, namely $A7^{Strep}_{PRD}$ and $A7_{PRD}$; each construct is designated by a circled number. (**B**) Microscopy images of condensates of ATTO-488-labeled $A7^{Strep}_{PRD}$; the circled number signifies the construct shown in panel **A**. (**C**) FRAP curves of $A7^{Strep}_{PRD}$ condensates; $n$ = 8, mean (solid line), SD (shaded region). (**D**) CR absorbance spectra of $A7_{PRD}$ aggregates (red), and freshly prepared solutions (blue); $n$ = 3. Fluorescence microscopy (**E**), TEM (**F**), and X-ray diffraction (**G**) of $A7_{PRD}$ fibrils. (**H**) Aggregation kinetics of $A7_{PRD}$, in the absence (grey) and presence (red) of calcium, monitored by ThT assay; $n$ = 3, mean (solid line), SD (shaded region). (**I**) Aggregation kinetics of $A7_{PRD}$ at different concentrations (n = 2, pH 7, 37 °C, non-agitated conditions, 5 mM $CaCl_2$); experimental data (circles), solid-lines (global fits carried out using model "secondary nucleation dominated, unseeded" in the program Amylofit)[43]. Inset shows a scheme of secondary nucleation process where nucleus comprising two monomers, grey circles, adds on to existing fibril.

**Supplementary Information**

## Materials and Methods

### Materials.

ATTO-647N maleimide was purchased from ATTO-TEC GmbH (catalog no. AD 647N-41) and was dissolved in dimethylformamide (DMF) at a concentration of ~11.5 mM. Streptavidin Alexa-Fluor488 conjugate was purchased from Thermo Fisher Scientific (catalog no. S32354). mPEG20K-Silane and Congo red (CR) were purchased from Sigma-Aldrich (catalog no. JKA3100 and C6277, respectively). Thioflavin T (ThT) and gels for sodium dodecyl sulfate polyacrylamide gel electrophoresis (SDS-PAGE; 4–12% Bis-Tris gels) were purchased from Thermo Fisher Scientific (catalog no. AC211760050, and NW04122BOX, respectively). Reagents for the preparation of giant unilamellar vesicles (GUVs), namely 1,2-dioleoyl-sn-glycero-3-phosphocholine (DOPC), 1,2-dioleoyl-sn-glycero-3-phospho-L-serine (DOPS), and 1,2-dipalmitoyl-sn-glycero-3-phosphoethanolamine-N-(lissamine rhodamine B sulfonyl) [i.e., 16:0 Liss Rhod PE], were purchased from Avanti polar lipids (catalog no. 850375, 840035, and 810158, respectively).

### Methods.

#### Recombinant protein expression and purification.

Codon-optimized A7 constructs, namely A7, $A7_{PRD}$, and $A7^{Strep}_{PRD}$, were custom synthesized from Azenta Life Sciences; see Fig. 10A for the design and mass-spectrometry (MS) analysis and Table 1 for subcloning of each construct. A7 was expressed with a tobacco etch virus (TEV) cleavable C-terminal twin-strep tag.[46] The primary sequence of the twin-strep tag is as follows: GSGSGSGSAWSHPQFEKGGGSGGGSGGSAWSHPQFEK; underlined residues represent the

binding motif for strep-tactin, a derivative of streptavidin. Both truncated constructs, namely $A7_{PRD}$, and $A7^{Strep}_{PRD}$, were expressed with the N-terminal B1 domain of protein G (GB1) tag,[47] used to enhance the expression levels, followed by a spacer sequence, a polyhistidine (6xHis) affinity tag, and a TEV cleavage site. Additionally, $A7^{Strep}_{PRD}$ carried a non-cleavable C-terminal strep tag. The primary sequence of the strep tag is as follows: WSHPQFEK. All A7 plasmids reported in this study were deposited in the Addgene repository, https://www.addgene.org (accession no. 198635 [A7], 190066 [$A7_{PRD}$], and 190067 [$A7^{Strep}_{PRD}$]). The construct for TEV protease was a generous gift from David S. Waugh (NIH).

TEV protease was expressed at 37 °C as described previously.[48] All A7 constructs were expressed at 16 °C. Cells were grown at 37 °C in 1 L Luria-Bertani (LB; MP Biomedicals, catalog no. 3002-036) medium at natural isotopic abundance. About 30 min before induction, the temperature of the cell culture was reduced to 16 °C. Cells were induced with 1 mM isopropyl β-d-1-thiogalactopyranoside (IPTG) at an absorbance of 0.8 at 600 nm and harvested after ca. 24 h.

The purification scheme of TEV protease has been described previously.[48] A7 was purified using affinity chromatography (ÄKTA Pure protein purification system, Cytiva) whereas $A7_{PRD}$, and $A7^{Strep}_{PRD}$, were purified using a combination of affinity and size-exclusion chromatography (ÄKTA Pure and Start protein purification systems, Cytiva) and reverse-phase high-performance liquid chromatography (HPLC; 1260 Infinity II liquid chromatography system, Agilent Technologies). In the case of A7, cells were resuspended in a lysis buffer comprising 50 mM Tris, pH 8, 10 mM ethylenediaminetetraacetic acid (EDTA), and 5 mM β-mercaptoethanol (BME). Cells were lysed using an EmulsiFlex-C3 (Avestin) and cleared by centrifugation (48,380g, 30 min). The resultant supernatant was loaded onto a XK 16/20 chromatography column (Cytiva) prepacked with Strep-Tactin-XT Sepharose resin (Cytiva) pre-equilibrated with 50 mM Tris, pH 8.0, 10 mM EDTA, and

5 mM BME, and eluted in the same buffer containing 50 mM biotin. The eluted protein was mixed with recombinant TEV protease (molar ratio 50:1) to hydrolyze the C-terminal twin-strep tag. The reaction mixture was dialyzed overnight at 4 °C in a buffer comprising 25 mM (N-2-hydroxyethylpiperazine-N'-2-ethanesulfonic acid) [HEPES], and 1 mM (tris(2-carboxyethyl)phosphine) [TCEP]; Slide-A-Lyzer G2 dialysis cassettes (Thermo Fisher Scientific). The completion of proteolysis was assessed using SDS-PAGE electrophoresis. The hydrolyzed product was passed through Strep-Tactin-XT and HisTrap (Cytiva) columns, pre-equilibrated with the above-mentioned buffer used for dialysis. Relevant flow-through fractions were pooled, concentrated, and stored at -80 °C.

For $A7^{Strep}_{PRD}$, cells were resuspended in a lysis buffer comprising 50 mM Tris, pH 8, and 6 M guanidine hydrochloride (GdmCl). Cells were lysed by EmulsiFlex-C3 and cleared by centrifugation. The resultant supernatant was filtered through a 0.45 µm vacuum-driven filtration device (Stericup, Sigma-Aldrich) before being loaded onto a HisTrap column (Cytiva) pre-equilibrated with lysis buffer. Bound protein was washed with 10 column volumes of refolding buffer comprising 50 mM Tris, pH 8.0, and 250 mM NaCl and eluted in the same buffer containing 1 M imidazole. The eluted protein fractions were pooled and loaded onto a XK 16/20 chromatography column (Cytiva) prepacked with Strep-Tactin Sepharose resin (Cytiva) pre-equilibrated with 50 mM Tris, pH 8.0, and 250 mM NaCl, and eluted in the same buffer containing 2.5 mM d-desthiobiotin. The eluted protein was mixed with recombinant TEV protease (molar ratio 50:1) to hydrolyze the N-terminal GB1 fusion tag (completion of proteolysis was assessed using SDS-PAGE electrophoresis). The proteolysis reaction was carried out at room temperature (~20 h) and produced a poorly soluble hydrolyzed product. The precipitated product was solubilized by the addition of 6 M GdmCl and further purified using reverse-phase HPLC (Jupiter

10 μm C18 300 Å column) with a 25–42% acetonitrile gradient comprising 0.1% trifluoroacetic acid (TFA). The eluted protein fractions were pooled, lyophilized, and stored at -80 °C.

For $A7_{PRD}$, a similar lysis and HisTrap column purification procedures as described above for $A7^{Strep}_{PRD}$ were carried out. The eluted protein was further purified using size-exclusion chromatography on a HiLoad 26/600 Superdex 75 prep-grade column (Cytiva) pre-equilibrated with 50 mM Tris, pH 8.0, and 250 mM NaCl. Relevant $A7_{PRD}$ fractions were pooled and incubated with recombinant TEV protease to cleave off the N-terminal GB1 fusion tag. The hydrolyzed product was further purified by reverse-phase HPLC using the above-described conditions. Eluted $A7_{PRD}$ fractions were aliquoted, lyophilized, and stored at -80 °C.

All protein constructs were verified by mass-spectrometry (MS) as described before[18-19, 48].

**Sedimentation velocity analytical ultracentrifugation (AUC).**

Sedimentation velocity experiments on A7 were carried out at 50,000 rpm and 20 °C on a Beckman Coulter ProteomeLab XL-I analytical ultracentrifuge and an An-50-Ti rotor following standard protocols.[49] A7 stock solution was prepared as described above (see Recombinant protein expression and purification section). Samples were diluted to ~2 and ~7 μM using a buffer comprising 25 mM HEPES, pH 7, and 1 mM TCEP. Absorbance sedimentation data were collected at 280 nm and analyzed using our published protocols.[18, 48] Sedimentation profiles showed the presence of a monomeric A7.

**Fluorophore labeling and phase separation.**

In the case of A7, protein was mixed with a 3-molar equivalent of ATTO-647N maleimide in 25 mM HEPES, pH 7, and 1 mM TCEP. The reaction was allowed to proceed at 4 °C overnight. The excess dye was removed by PD midiTrap G-25 columns (Cytiva). This sample was mixed

with the corresponding unconjugated protein (concentration of fluorophore-labeled protein = 5 molar percent). 2 mM $CaCl_2$ was then added to induce phase separation of A7 and the resultant sample (final protein concentration = 40 μM) was visualized using fluorescence microscopy (see below).

For $A7^{Strep}_{PRD}$, the lyophilized protein was dissolved in a small volume of dimethylsulfoxide (DMSO) and diluted immediately in a buffer containing 25 mM HEPES and 5 mM $CaCl_2$ to induce phase separation (final protein concentration = 50 μM). 0.02 mg/mL Streptavidin Alexa-Fluor488 conjugate was then added to this solution, which was visualized using fluorescence microscopy (see below).

**GUV preparation.**

GUVs were prepared using the inverted emulsion method.[50] Briefly, for the oil phase, the chloroform solutions of DOPC, DOPS, and 16:0 Liss Rhod PE were mixed in a glass vial under dark conditions (69.5, 30, and 0.5%, respectively). The resultant mixture was dried under nitrogen, followed by vacuum desiccation (vacuum oven; VWR) for ~2 h at room temperature. 1 mL of mineral oil (Thermo Fisher Scientific, catalog no. O121-1) was added to the vial and sonicated for 1 h at room temperature. For the aqueous phase, phosphate buffered saline (PBS; osmolarity: 280 mOsm, pH 7.4) was mixed with Ficoll 400 (Sigma-Aldrich; 35% w/v in water) to give a final concentration of 3.5% Ficoll-400. 10 μL of this solution was added to 100 μL oil phase and emulsified. The emulsion was then mixed with the aqueous phase, followed by centrifugation (10,000g, 10 min, 4 °C). The GUVs at the bottom of the tube were collected and stored at 4 °C for further analysis.

**Microscopy imaging and FRAP assays.**

Microscopy imaging and FRAP assays were carried out using our previously published protocols.[20-22] Briefly, differential interference contrast (DIC) imaging was performed on a Nikon Ti2 widefield microscope equipped with a DS-Qi2 CMOS camera and 100x/1.49NA oil DIC N2 Objective; Nikon Imaging Center, UC San Diego. The condenser prism and the polarizer cube were controlled by the Nikon Elements software. Samples of A7 condensates were excited by a 640 nm laser controlled by a Lumencor SpectraX for imaging of ATTO-647N. In the case of $A7_{PRD}^{Strep}$ + Streptavidin Alexa-Fluor488 mixtures, a 488 nm laser was used. Microscopy image of aged droplets of $A7_{PRD}$ shown in Fig. 7E, was acquired using a similar procedure. Briefly, droplets of 50 μM $A7_{PRD}$ with 20 μM ThT were incubated at 37 ºC for one day. Images were taken using a 488 nm laser.

For microscopy experiments, slides were passivated using PEG-silane.[21, 51] Briefly, slides were cleaned by sonication in 3% v/v Hellmanex III (Sigma-Aldrich), rinsed in 0.5 M NaOH, dried using a nitrogen stream, and placed in a vacuum oven (VWR) at 90 °C for 10 min. PEG-Silane was dissolved in DMSO at 5% w/v and was sandwiched between the slide and coverslip, and incubated at 90 °C for 20 min. Passivated slides were subsequently rinsed with water and dried with a nitrogen stream. Imaging chambers composed of two passivated coverslips and a 9-mm silicone mold (Grace BioLabs) were used for all microscopy analyses.

FRAP measurements of ATTO-647N-labeled A7 were performed on a Nikon point scanning confocal C2 with 2 GaAsP PMTs using a Plan Apo λ 100x/1.45 NA Oil objective. Photobleaching of each sample was achieved using 2 iterations of 50% 640 nm laser power directed at the bleaching area for 10 s, and subsequent recovery was imaged at 2 s intervals over 150 frames using 0.1% 640 nm laser power. Images were corrected for background fluorescence, and intensity from the bleached region was normalized against an unbleached region on a nearby condensate of

similar size and intensity. A similar procedure was used for $A7^{Strep}_{PRD}$ + Streptavidin Alexa-Fluor488 mixtures, except for the use of 488 nm laser.

**CR Assay.**

CR assay was carried out as described previously.[18-19, 21] Briefly, CR was dissolved in MilliQ water (MilliQ IQ 7000 purification system, Millipore–Sigma). CR stock solution (0.2% w/v) was filtered through a 0.22 μm filter and used immediately. $A7_{PRD}$ samples were prepared by dissolving ~1 mg lyophilized protein in 20 μL DMSO and diluting this solution to 50 μM using a buffer comprising 25 mM HEPES, pH 7.0, and 5 mM $CaCl_2$. These freshly prepared samples were mixed with CR stock solution (50:1 dilution; protein vs. CR). Additionally, samples of $A7_{PRD}$ were incubated for ~3 h at room temperature to induce fibrillization, followed by mixing with CR stock solution (same dilution as above). In both cases, the absorption spectra of three replicates were measured using an DeNovix DS-11+ (M/C) Spectrophotometer.

**Transmission electron microscopy (TEM).**

TEM samples of fibrils of A7 and $A7_{PRD}$ constructs were prepared using our published protocols.[18-19] TEM images were acquired using a JEM-1400 Plus transmission electron microscope (JEOL) and recorded on a OneView digital camera (Gatan), Electron Microscopy Core Facility, UC San Diego.

**X-ray diffraction.**

X-ray diffraction was carried out as described previously.[21] A 50 μM stock solution of $A7_{PRD}$ was incubated at 37 °C for a week. $A7_{PRD}$ fibrils were pelleted for 30 min at 259,000g and 20°C using Optima XE Ultracentrifuge and SW 55 Ti swinging bucket rotor (Beckman Coulter). A small amount of the sample was dried and loaded onto a Cryoloop. The sample was mounted on a Bruker

Microstar 592 diffractometer equipped with an APEX II CCD detector and Cu Kα radiation (λ = 1.54178 Å); UC San Diego Crystallography Facility. X-ray data was collected using a 360° ϕ scan with an exposure time of 300 s.

**Fibril formation and dissolution kinetics.**

In the case of $A7_{PRD}$, samples were prepared by dissolving the lyophilized $A7_{PRD}$ in DMSO and rapidly diluting the DMSO stock in a buffer comprising 25 mM HEPES, pH 7, and 5 mM $CaCl_2$ to achieve final concentrations ranging from 5–50 μM. Measurements were carried out at 37 °C under non-agitated conditions using a microplate reader (Infinite M Plex; Tecan) and sealed 96-well flat bottom plates (Corning; catalog no. 3370) containing 100 μl sample per well. ThT (20 μM) fluorescence was recorded as a function of time. Excitation and emission wavelengths were 415 and 480 nm, respectively. For A7, similar experimental conditions were used, except that measurements were carried out with continuous linear shaking (1.5 mm, 335.8 rpm). Global fitting of the experimental ThT curves for $A7_{PRD}$ was carried out using the protocol described by Meisl et al.[43]

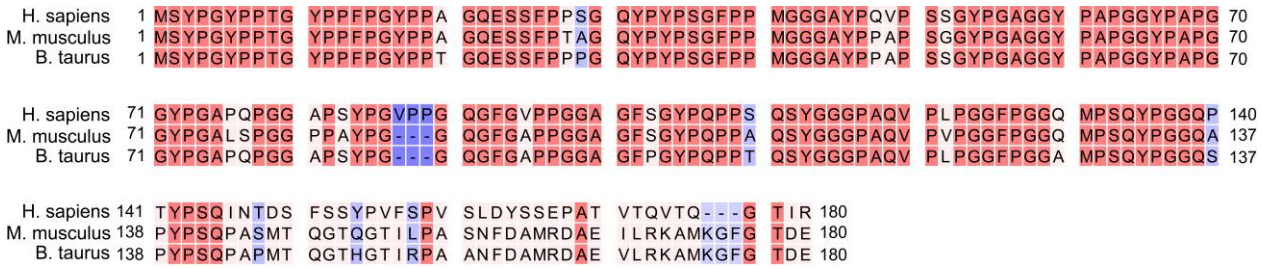


**Figure 8. Primary sequence comparison of representative A7-head domains among vertebrate species.** A blue-to-red gradient is used to denote conservation, with blue and red colors depicting the least and most conserved residues, respectively. The following sequences were used for analysis: H. sapiens (Uniprot accession no. P20073), M. musculus (Uniprot accession no. Q07076), and B. taurus (Uniprot accession no. P20072).

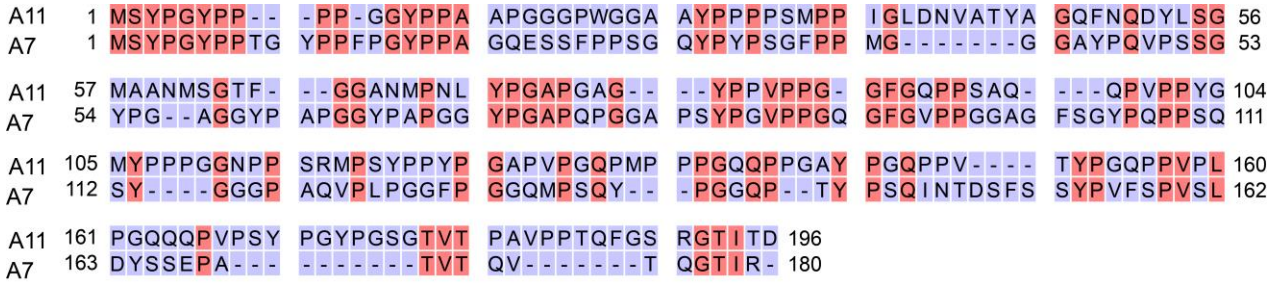


**Figure 9. Primary sequence comparison of head domains of A7 and A11.** Same color gradient as Fig. 8. The uniprot accession no. for A11 is P50995.

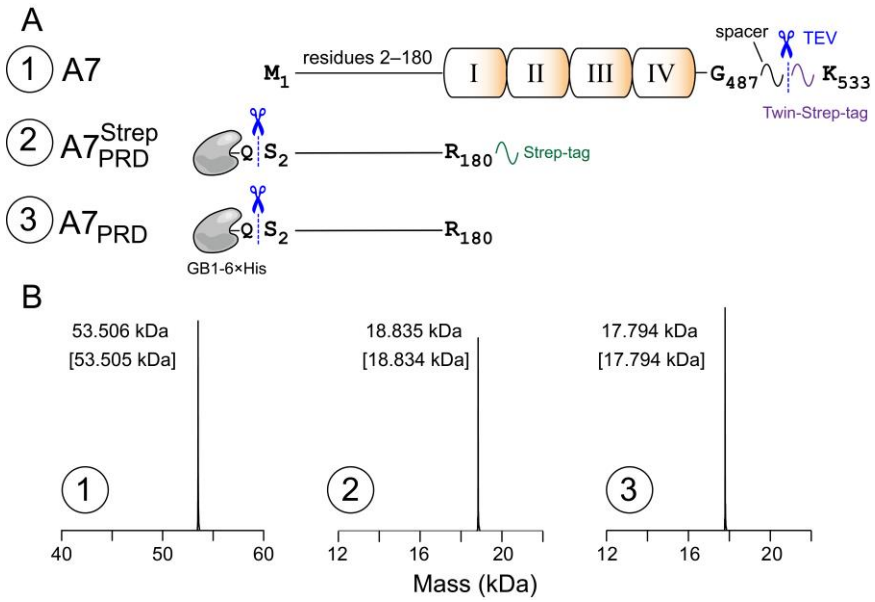


**Figure 10. Recombinant A7 constructs used in current study.** (**A**) List of recombinant A7 constructs, namely A7, $A7_{PRD}^{Strep}$ and $A7_{PRD}$. Each construct is designated by a circled number. The locations of the TEV cleavage sites are marked by blue vertical dashed lines and scissors. In the case of A7 (construct no. 1), the TEV cleavage site is located at the C-terminus, sandwiched between a spacer sequence (SGSENLYFQ) and the twin-strep tag[46]. Note that native residue Q488 of A7 was not included in this construct to accommodate the spacer and TEV cleavage site. For the truncated constructs, GB1-6xHis denotes the N-terminal GB1 tag, used to enhance the expression levels, followed by a spacer sequence and a polyhistidine (6xHis) affinity tag. Additionally, $A7_{PRD}^{Strep}$ (construct no. 2) carried a non-cleavable C-terminal strep tag[52]. (**B**) Analysis of TEV-cleaved constructs (same numbering as panel **A**) using liquid chromatography–electrospray ionization–time-of-flight mass spectrometry (LC–ESI–TOFMS); the numbers in parenthesis represent the corresponding theoretical masses.

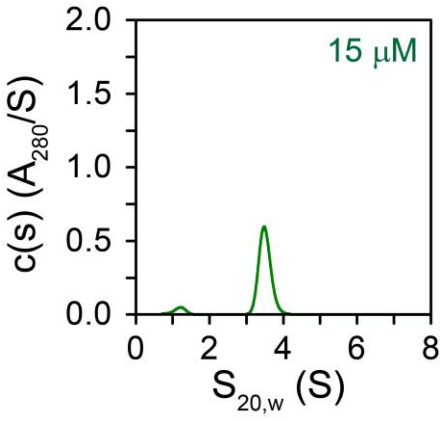


**Figure 11. Sedimentation analysis of recombinant A7.** Absorbance sedimentation c(s) profiles of recombinant A7 (15 μM). All measurements were carried out at 20 ºC in 25 mM HEPES, pH 7, and 1 mM TCEP. Note that unlike the profiles shown in Fig. 1C (main text) that were acquired using 12 mm cell, the above data were acquired using 3 mm cell.


**Figure 12. Confocal microscopy analysis of membrane binding properties of A7.** GUVs were made using DOPC (99.95%) and spiked with 16:1 Liss Rhod PE dye (0.05%). The concentration of ATTO-647N-labeled A7 was 200 nM. The buffer conditions were as follows: 25 mM HEPES, pH 7, and 100 nM calcium. Representative microscopy images of the respective fluorescent channels and their overlay are shown. The lack of fluorescence signal from A7 at the membrane surface indicated that A7 did not colocalize with zwitterionic GUVs containing DOPC.

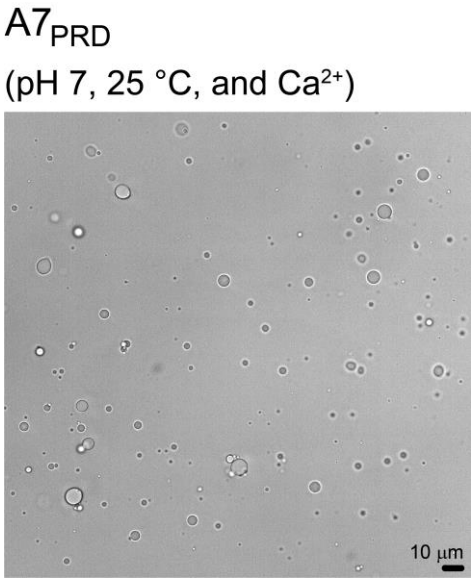


**Figure 13. DIC images of droplets made by $A7_{PRD}$.** Images were acquired at 25 °C. The buffer composition as follows: 25 mM HEPES, pH 7, and 5 mM calcium.

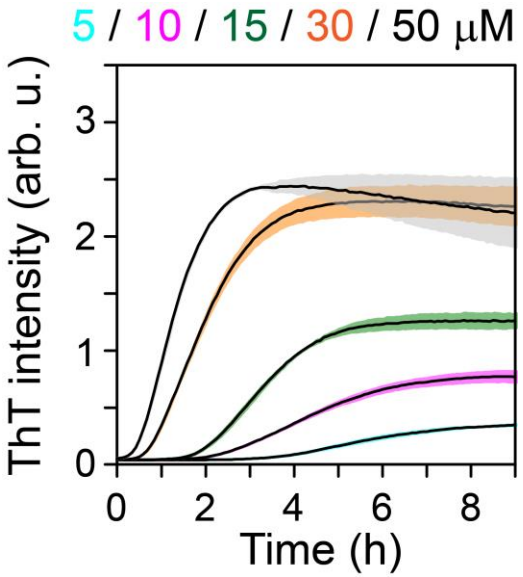


**Figure 14. Aggregation kinetics of $A7_{PRD}$.** ThT fluorescence was monitored to determine the effects of concentration on the aggregation kinetics of $A7_{PRD}$, $n = 3$, mean (solid line), SD (shaded region). All measurements were carried out at 37 °C under non-agitated conditions. The buffer composition as follows: 25 mM HEPES, pH 7, 5 mM calcium, and 20 μM ThT.

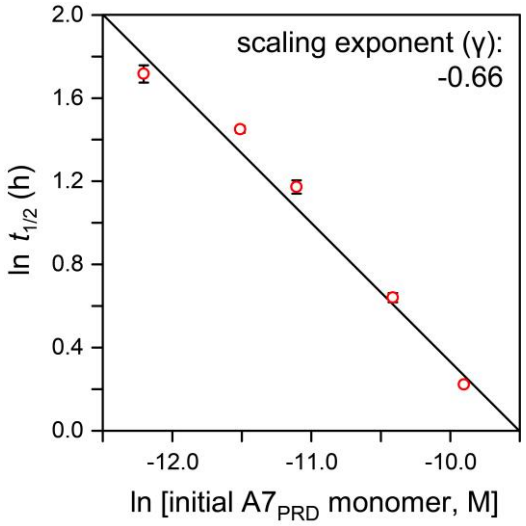


**Figure 15. Dependence of half-times, $t_{1/2}$, on the initial monomer concentration of $A7_{PRD}$.** Double logarithmic plot, log $t_{1/2}$ = γlog[$m_0$] + constant, where γ is the scaling exponent and $m_0$ is $A7_{PRD}$ monomer at time 0. The raw data used to generate this plot is shown in Fig. 14. The values of $t_{1/2}$ and γ were extracted using the program Amylofit[43] by fitting the power-law function, $t_{1/2} \sim [m_0]^{\gamma}$. The obtained value of γ (i.e., -0.66) suggests that in the case of $A7_{PRD}$ fibrillization, the primary nucleation process is partially dependent on initial monomer concentration, whereas the secondary process of fibril propagation is independent of monomer concentration.

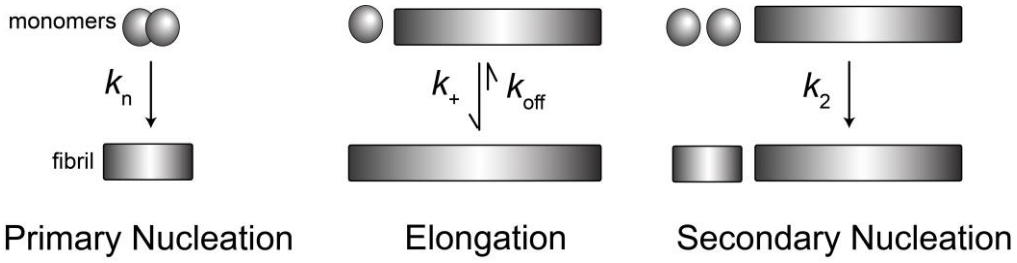


**Figure 16. Microscopic processes involved in protein fibrillization, and the associated rate constants.** Adapted from Meisl et al.[43]

**Table 1. Recombinant constructs used in current study[a,b].**

| Construct | Addgene accession no. | Competenet cells | Induction temperature | Yield[c] (mg/L) |
|---|---|---|---|---|
| A7 | 198635 | BL(21)DE3 | 16 °C | 15 mg/L |
| $A7_{PRD}$ | 190066 | BL(21)DE3 | 16 °C | 30 mg/L |
| $A7^{Strep}_{PRD}$ | 190067 | BL(21)DE3 | 16 °C | 25 mg/L |

a) BL21(DE3) cells were obtained from Agilent (catalog no. 200131).

b) Cultures were grown in LB media overnight upon induction with 1 mM IPTG. LB capsules were obtained from MP Biomedicals (catalog no. 3002-036), and were used according to the manufacturers' protocols.

c) The yield represents the total amount of TEV-cleaved protein obtained from a liter of bacterial culture.

## ASSOCIATED CONTENT

Human Annexin A7 (Uniprot accession no. P20073). All A7 plasmids reported in this study were deposited in the Addgene repository, https://www.addgene.org (accession no. 198635 [A7], 190066 [$A7_{PRD}$], 190067 [$A7^{Strep}_{PRD}$]).


## ACKNOWLEDGEMENTS

Chapter 1, in full, has been submitted for publication of the material as it may appear in Biochemistry, 2023, Yu Chenrong, Nelson L. Spencer; Ghirlando Rodolfo; Deshmukh, Lalit. "Phase separation and fibrillization of human annexin A7 is mediated by its proline-rich domain". The -author of the thesis was the primary researcher and author of this paper.

# CONCLUSION

Liquid-liquid phase separation of proteins and nucleic acids is responsible for the formation of multiple membraneless organelles, including stress granules, P bodies, nucleoli, Cajal bodies, and many others. Aberrations in phase separation are likely a vital contributing factor to the formation of amyloid fibrils that are associated with many proteinopathies. Thus, understanding how these condensates form, their regulation and function, and the molecular details of their fibrillar transitions will shed light on the dynamic interplay between cellular processes controlled by these condensates and the corresponding pathology. In this study, we uncovered that recombinant annexin A7, a human protein belonging to the annexin superfamily of calicium and phospholipid binding proteins, phase separates into nondynamic condensates that slowly transition into amyloid fibrils. We show that the head domain of A7, comprising 180 residues and 25% prolines ($A7_{PRD}$) is likely responsible for the aggregation of full-length A7. A7 is known to self-associate and promote membrane aggregation and fusion events in the presence of calcium. Prior studies have ascribed these properties to the extreme N-terminal residues of $A7_{PRD}$. The results presented in our study are consistent with these known observations. Moreover, the aggregation properties of A7 are similar to those of another member of the annexin family, annexin A11 and its proline-rich head domain. Thus, we speculate that the phase-separation properties of A7 and A11 will play a vital role in regulating their cellular functions, and we are actively investigating these physiological processes in our laboratory. Fibrillization and aggregation of A11 are linked with ALS. Specifically, four missense point mutations in its proline-rich head domain have been shown to generate A11 inclusions in ALS patients. We therefore speculate that aberrant fibrillization of A7 would also result in pathology, such as A7-associated cancers. The amyloid fibrils formed by A11 were labile and slowly dissolved upon the addition of its binding partner, namely S100A6. Studies to determine whether A7 fibrils exhibit a similar dissolution pattern in the presence of its known binding partners, namely sorcin, SODD, and ALG-2, are currently ongoing in our laboratory. Finally, we note that the aggregation properties of $A7_{PRD}$ are also similar to those of

another PRD discovered in our laboratory, belonging to the human protein ALIX, which was shown to phase separate and form amyloid fibrils. Therefore, although eukaryotic PRDs are known to form dynamic cell signaling networks, PRDs of A7, A11, and ALIX may represent a new subclass of PRDs that can phase separate and form amyloid fibrils.

REFERENCES


(1) Mitrea, D. M.; Kriwacki, R. W., Phase separation in biology; functional organization of a higher order. *Cell Commun. Signal.* **2016,** *14* (1), 1.

(2) Boeynaems, S.; Alberti, S.; Fawzi, N. L.; Mittag, T.; Polymenidou, M.; Rousseau, F.; Schymkowitz, J.; Shorter, J.; Wolozin, B.; Van Den Bosch, L.; Tompa, P.; Fuxreiter, M., Protein phase separation: A new phase in cell biology. *Trends Cell Biol.* **2018,** *28* (6), 420-435.

(3) Gomes, E.; Shorter, J., The molecular language of membraneless organelles. *J. Biol. Chem.* **2019,** *294* (18), 7115-7127.

(4) Wagner, R.; Barry, M., Some remarks and inquiries concerning the germinal vesicle (Vesicula Germinativa.). *Edinb. Med. Surg. J.* **1836,** *45* (127), 423-426.

(5) Li, P.; Banjade, S.; Cheng, H.-C.; Kim, S.; Chen, B.; Guo, L.; Llaguno, M.; Hollingsworth, J. V.; King, D. S.; Banani, S. F.; Russo, P. S.; Jiang, Q.-X.; Nixon, B. T.; Rosen, M. K., Phase transitions in the assembly of multivalent signalling proteins. *Nature* **2012,** *483* (7389), 336-340.

(6) Li, J.; Zhang, M.; Ma, W.; Yang, B.; Lu, H.; Zhou, F.; Zhang, L., Post-translational modifications in liquid-liquid phase separation: a comprehensive review. *Mol. Biomed.* **2022,** *3* (1), 13.

(7) Alberti, S. Phase separation in biology. *Curr Biol.* **2017**, 27(20), R1097-R1102.

(8) Brangwynne, C. P.; Eckmann, C. R.; Courson, D. S.; Rybarska, A.; Hoege, C.; Gharakhani, J.; Jülicher, F.; Hyman, A. A., Germline P granules are liquid droplets that localize by controlled dissolution/dondensation. *Science* **2009,** *324* (5935), 1729-1732.

(9) Shin, Y.; Brangwynne, C. P., Liquid phase condensation in cell physiology and disease. *Science* **2017,** *357* (6357), eaaf4382.

(10) Lu, J.; Qian, J.; Xu, Z.; Yin, S.; Zhou, L.; Zheng, S.; Zhang, W., Emerging roles of liquid–liquid phase separation in cancer: From protein aggregation to immune-associated signaling. *Front. Cell Dev. Biol.* **2021,** *9*.

(11) Zbinden, A.; Pérez-Berlanga, M.; De Rossi, P.; Polymenidou, M., Phase separation and neurodegenerative diseases: A disturbance in the force. *Dev. Cell* **2020,** *55* (1), 45-68.

(12) Patel, A.; Lee, Hyun O.; Jawerth, L.; Maharana, S.; Jahnel, M.; Hein, Marco Y.; Stoynov, S.; Mahamid, J.; Saha, S.; Franzmann, Titus M.; Pozniakovski, A.; Poser, I.; Maghelli, N.; Royer, Loic A.; Weigert, M.; Myers, Eugene W.; Grill, S.; Drechsel, D.; Hyman, Anthony A.; Alberti, S., A liquid-to-solid phase transition of the ALS protein FUS accelerated by disease mutation. *Cell* **2015,** *162* (5), 1066-1077.

(13) Molliex, A.; Temirov, J.; Lee, J.; Coughlin, M.; Kanagaraj, Anderson P.; Kim, Hong J.; Mittag, T.; Taylor, J. P., Phase separation by low complexity domains promotes stress granule assembly and drives pathological fibrillization. *Cell* **2015,** *163* (1), 123-133.

(14) Chiti, F.; Dobson, C. M., Protein misfolding, amyloid formation, and human disease: A summary of progress over the last decade. *Annu. Rev. Biochem.* **2017,** *86*, 27-68.

(15) Kim, H. J.; Kim, N. C.; Wang, Y.-D.; Scarborough, E. A.; Moore, J.; Diaz, Z.; MacLea, K. S.; Freibaum, B.; Li, S.; Molliex, A.; Kanagaraj, A. P.; Carter, R.; Boylan, K. B.; Wojtas, A. M.; Rademakers, R.; Pinkus, J. L.; Greenberg, S. A.; Trojanowski, J. Q.; Traynor, B. J.; Smith, B. N.; Topp, S.; Gkazi, A.-S.; Miller, J.; Shaw, C. E.; Kottlors, M.; Kirschner, J.; Pestronk, A.; Li, Y. R.; Ford, A. F.; Gitler, A. D.; Benatar, M.; King, O. D.; Kimonis, V. E.; Ross, E. D.; Weihl, C. C.; Shorter, J.; Taylor, J. P., Mutations in prion-like domains in hnRNPA2B1 and hnRNPA1 cause multisystem proteinopathy and ALS. *Nature* **2013,** *495* (7442), 467-473.

(16) Kiessling, L. L.; Lamanna, A. C. In *Multivalency in Biological Systems*, Dordrecht, Springer Netherlands: Dordrecht, 2003; pp 345-357.

(17) van der Lee, R.; Buljan, M.; Lang, B.; Weatheritt, R. J.; Daughdrill, G. W.; Dunker, A. K.; Fuxreiter, M.; Gough, J.; Gsponer, J.; Jones, D. T.; Kim, P. M.; Kriwacki, R. W.; Oldfield, C. J.; Pappu, R. V.; Tompa, P.; Uversky, V. N.; Wright, P. E.; Babu, M. M., Classification of intrinsically disordered regions and proteins. *Chem. Rev.* **2014,** *114* (13), 6589-6631.

(18) Elias, R. D.; Ma, W.; Ghirlando, R.; Schwieters, C. D.; Reddy, V. S.; Deshmukh, L., Proline-rich domain of human ALIX contains multiple TSG101-UEV interaction sites and forms phosphorylation-mediated reversible amyloids. *Proc. Natl. Acad. Sci. U.S.A.* **2020,** *117* (39), 24274-24284.

(19) Elias, R. D.; Ramaraju, B.; Deshmukh, L., Mechanistic roles of tyrosine phosphorylation in reversible amyloids, autoinhibition, and endosomal membrane association of ALIX. *J. Biol. Chem.* **2021,** *297* (5), 101328.

(20) Elias, R. D.; Zhu, Y.; Su, Q.; Ghirlando, R.; Zhang, J.; Deshmukh, L., Reversible phase separation of ESCRT-protein ALIX through tyrosine phosphorylation. **under revision**.

(21) Shihora, A.; Elias, R. D.; Hammond, J. A.; Ghirlando, R.; Deshmukh, L., ALS variants of annexin A11's proline-rich domain impair its S100A6-mediated fibril dissolution. **under revision**.

(22) Nelson, S. L.; Li, Y.; Chen, Y.; Deshmukh, L., Avidity-Based Method for the Efficient Generation of Monoubiquitinated Recombinant Proteins. *J. Am. Chem. Soc.* **2023,** *145* (14), 7748-7752.

(23) Gerke, V.; Moss, S. E., Annexins: From structure to function. *Physiol. Rev.* **2002,** *82* (2), 331-371.

(24) Moss, S. E.; Morgan, R. O., The annexins. *Genome Biol.* **2004,** *5* (4), 219.

(25) Grewal, T.; Wason, S. J.; Enrich, C.; Rentero, C., Annexins - insights from knockout mice. *Biol. Chem.* **2016,** *397* (10), 1031-53.

(26) Weisz, J.; Uversky, V. N., Zooming into the dark Side of human annexin-S100 complexes: Dynamic alliance of flexible partners. *Int. J. Mol. Sci.* **2020,** *21* (16), 5879.

(27) Liao, Y.-C.; Fernandopulle, M. S.; Wang, G.; Choi, H.; Hao, L.; Drerup, C. M.; Patel, R.; Qamar, S.; Nixon-Abell, J.; Shen, Y.; Meadows, W.; Vendruscolo, M.; Knowles, T. P. J.; Nelson, M.; Czekalska, M. A.; Musteikyte, G.; Gachechiladze, M. A.; Stephens, C. A.; Pasolli, H. A.; Forrest, L. R.; St George-Hyslop, P.; Lippincott-Schwartz, J.; Ward, M. E., RNA granules hitchhike on lysosomes for long-distance transport, using annexin A11 as a molecular tether. *Cell* **2019,** *179* (1), 147-164.e20.

(28) Enrich, C.; Rentero, C.; Meneses-Salas, E.; Tebar, F.; Grewal, T., Annexins: Ca2+ Effectors Determining Membrane Trafficking in the Late Endocytic Compartment. In *Membrane Dynamics and Calcium Signaling*, Krebs, J., Ed. Springer International Publishing: Cham, 2017; pp 351-385.

(29) Smith, B. N.; Topp, S. D.; Fallini, C.; Shibata, H.; Chen, H. J.; Troakes, C.; King, A.; Ticozzi, N.; Kenna, K. P.; Soragia-Gkazi, A.; Miller, J. W.; Sato, A.; Dias, D. M.; Jeon, M.; Vance, C.; Wong, C. H.; de Majo, M.; Kattuah, W.; Mitchell, J. C.; Scotter, E. L.; Parkin, N. W.; Sapp, P. C.; Nolan, M.; Nestor, P. J.; Simpson, M.; Weale, M.; Lek, M.; Baas, F.; Vianney de Jong, J. M.; Ten Asbroek, A.; Redondo, A. G.; Esteban-Pérez, J.; Tiloca, C.; Verde, F.; Duga, S.; Leigh, N.; Pall, H.; Morrison, K. E.; Al-Chalabi, A.; Shaw, P. J.; Kirby, J.; Turner, M. R.; Talbot, K.; Hardiman, O.; Glass, J. D.; De Belleroche, J.; Maki, M.; Moss, S. E.; Miller, C.; Gellera, C.; Ratti, A.; Al-Sarraj, S.; Brown, R. H., Jr.; Silani, V.; Landers, J. E.; Shaw, C. E., Mutations in the vesicular trafficking protein annexin A11 are associated with amyotrophic lateral sclerosis. *Sci. Transl. Med.* **2017,** *9* (388).

(30) Creutz, C. E.; Pazoles, C. J.; Pollard, H. B., Identification and purification of an adrenal medullary protein (synexin) that causes calcium-dependent aggregation of isolated chromaffin granules. *J. Biol. Chem.* **1978,** *253* (8), 2858-66.

(31) Creutz, C. E.; Pazoles, C. J.; Pollard, H. B., Self-association of synexin in the presence of calcium. Correlation with synexin-induced membrane fusion and examination of the structure of synexin aggregates. *J. Biol. Chem.* **1979,** *254* (2), 553-8.

(32) Brownawell, A. M.; Creutz, C. E., Calcium-dependent binding of sorcin to the N-terminal domain of synexin (annexin VII). *J. Biol. Chem.* **1997,** *272* (35), 22182-22190.

(33) Creutz, C. E., Novel protein ligands of the annexin A7 N-terminal region suggest pro-beta helices engage one another with high specificity. *Gen. Physiol. Biophys.* **2009,** *28 Spec No Focus* (Spec), F7-f13.

(34) Satoh, H.; Nakano, Y.; Shibata, H.; Maki, M., The penta-EF-hand domain of ALG-2 interacts with amino-terminal domains of both annexin VII and annexin XI in a Ca2+-dependent manner. *Biochim. Biophys. Acta* **2002,** *1600* (1-2), 61-7.

(35) Sønder, S. L.; Boye, T. L.; Tölle, R.; Dengjel, J.; Maeda, K.; Jäättelä, M.; Simonsen, A. C.; Jaiswal, J. K.; Nylandsted, J., Annexin A7 is required for ESCRT III-mediated plasma membrane repair. *Sci. Rep.* **2019,** *9* (1), 6726.

(36) Naidu, D. G.; Raha, A.; Chen, X.-L.; Spitzer, A. R.; Chander, A., Partial truncation of the NH2-terminus affects physical characteristics and membrane binding, aggregation, and fusion properties of annexin A7. *Biochim. Biophys. Acta - Mol. Cell Biol. Lipids* **2005,** *1734* (2), 152-168.

(37) Chander, A.; Naidu, D. G.; Chen, X.-L., A ten-residue domain (Y11–A20) in the NH2-terminus modulates membrane association of annexin A7. *Biochim. Biophys. Acta - Mol. Cell Biol. Lipids* **2006,** *1761* (7), 775-784.

(38) Tokumitsu, H.; Mizutani, A.; Minami, H.; Kobayashi, R.; Hidaka, H., A calcyclin-associated protein is a newly identified member of the $Ca^{2+}$/phospholipid-binding proteins, annexin family. *J. Biol. Chem.* **1992,** *267* (13), 8919-24.

(39) Hong, K.; Düzgüneş, N.; Papahadjopoulos, D., Role of synexin in membrane fusion. Enhancement of calcium-dependent fusion of phospholipid vesicles. *J. Biol. Chem.* **1981,** *256* (8), 3641-4.

(40) Hong, K.; Düzgüneş, N.; Ekerdt, R.; Papahadjopoulos, D., Synexin facilitates fusion of specific phospholipid membranes at divalent cation concentrations found intracellularly. *Proc. Natl. Acad. Sci. U.S.A.* **1982,** *79* (15), 4642-4.

(41) Li, H.; Rahimi, F.; Sinha, S.; Maiti, P.; Bitan, G.; Murakami, K., Amyloids and protein aggregation—Analytical methods. In *Encyclopedia of Analytical Chemistry*.

(42) Morris, K. L.; Serpell, L. C., X-ray fibre diffraction studies of amyloid fibrils. *Methods Mol. Biol.* **2012,** *849*, 121-35.

(43) Meisl, G.; Kirkegaard, J. B.; Arosio, P.; Michaels, T. C. T.; Vendruscolo, M.; Dobson, C. M.; Linse, S.; Knowles, T. P. J., Molecular mechanisms of protein aggregation from global fitting of kinetic models. *Nat. Protoc.* **2016,** *11* (2), 252-272.

(44) Meisl, G.; Yang, X.; Hellstrand, E.; Frohm, B.; Kirkegaard, J. B.; Cohen, S. I. A.; Dobson, C. M.; Linse, S.; Knowles, T. P. J., Differences in nucleation behavior underlie the contrasting aggregation kinetics of the Aβ40 and Aβ42 peptides. *Proc. Natl. Acad. Sci. U.S.A.* **2014,** *111* (26), 9384-9389.

(45) Sen, N.; Spitzer, A. R.; Chander, A., Calcium-dependence of synexin binding may determine aggregation and fusion of lamellar bodies. *Biochem. J.* **1997,** *322* (1), 103-109.

(46) Schmidt, T. G. M.; Batz, L.; Bonet, L.; Carl, U.; Holzapfel, G.; Kiem, K.; Matulewicz, K.; Niermeier, D.; Schuchardt, I.; Stanar, K., Development of the Twin-Strep-tag and its application for purification of recombinant proteins from cell culture supernatants. *Protein Expr. Purif.* **2013,** *92* (1), 54-61.

(47) Huth, J. R.; Bewley, C. A.; Jackson, B. M.; Hinnebusch, A. G.; Clore, G. M.; Gronenborn, A. M., Design of an expression system for detecting folded protein domains and mapping macromolecular interactions by NMR. *Protein Sci.* **1997,** *6* (11), 2359-64.

(48) Ramaraju, B.; Nelson, S. L.; Zheng, W.; Ghirlando, R.; Deshmukh, L., Quantitative NMR Study of Insulin-Degrading Enzyme Using Amyloid-beta and HIV-1 p6 Elucidates Its Chaperone Activity. *Biochemistry* **2021,** *60* (33), 2519-2523.

(49) Zhao, H.; Brautigam, C. A.; Ghirlando, R.; Schuck, P., Overview of current methods in sedimentation velocity and sedimentation equilibrium analytical ultracentrifugation. *Curr. Protoc. Protein Sci.* **2013,** *Chapter 20*, Unit20.12.

(50) Pautot, S.; Frisken, B. J.; Weitz, D. A., Production of unilamellar vesicles using an inverted emulsion. *Langmuir* **2003,** *19* (7), 2870-2879.

(51) Gidi, Y.; Bayram, S.; Ablenas, C. J.; Blum, A. S.; Cosa, G., Efficient one-step PEG-silane passivation of glass surfaces for single-molecule fluorescence studies. *ACS Appl. Mater. Interfaces* **2018,** *10* (46), 39505-39511.

(52) Schmidt, T. G. M.; Skerra, A., The Strep-tag system for one-step purification and high-affinity detection or capturing of proteins. *Nat. Protoc.* **2007,** *2* (6), 1528-1535.